Archives of Civil and Mechanical Engineering (2023) 23:5
https://doi.org/10.1007/s43452-022-00525-2

ORIGINAL ARTICLE

Low velocity perforation of thick magnesium alloy AM60 plates impacted by rigid conical-nose impactor

Zdzisław Nowak[1] · **Zbigniew L. Kowalewski**[2] · **Tadeusz Szymczak**[3]

Received: 2 March 2022 / Revised: 26 August 2022 / Accepted: 3 September 2022 / Published online: 13 October 2022

Abstract
The impact resistance behaviour of the plate made of the AM60 magnesium alloy at the low velocity impact perforation mode is here investigated at room temperature using a numerical approach based on experimental results. Dynamic tests were performed using an impact digital tower on the 10.0 mm thick AM60 magnesium alloy plates using cylindrical impactors with conical-nose shapes of a nominal diameter of 12.0 mm, and a nominal mass of 5.77 kg. The plates were impacted with velocities ranging from 7 to 16 m/s. During the experiments, the failure of the target plates was evaluated. Finite element (FE) model was validated using experimental results. FE simulations of the conducted experiments were performed with ABAQUS software. In simulations the strain rate dependent Johnson–Cook yield criterion with a strain hardening law was accompanied with either the ductile fracture criterion or stress triaxiality-dependent JC fracture criterion to describe the target material properties. The stress and strain distributions for different impactor velocity considered were calculated using initial impact velocity data obtained from the experiments. A range of parameters, like element size, the fracture initiation strain, friction coefficient, etc. which play an important role in the simulation, were studied. The results of numerical simulation were compared with those from the experiment obtained. A good agreement between them was achieved. The failure process of AM60 target-plate revealed that in the case of the conical-nose impactor, the ductile hole enlargement occurs during the initial stage of the impact, and subsequently, a through-thickness fracture develops causing its shear plugging failure.

Keywords AM60 magnesium alloy · Room temperature impact drop-weight tower experiment · Conical-shape impactor · Numerical study of perforation process · Elastic-viscoplastic numerical analysis

1 Introduction

Metal plates of the high strength steel, aluminium, titanium and magnesium alloy are widely used in protective structures against low, medium and high velocity impacts. Physical mechanisms of a penetration metal target-plates by almost rigid-impactor depend on the target materials, impact velocity, impactor nose shape, target boundary conditions, relative dimensions of a impactor and target-plate. Arias et al. [1] using numerical simulations exhibited, that the impact failure mode depends on the impactor nose shape. In the case of conical-nose impactors the permanent radial compression and hole enlargement were observed. Using numerical methods the phenomena of normal and oblique impact of sharp-nose impactors on ductile targets can be investigated [2]. The plate targets in form of the steel plates with a thickness of 12 mm or aluminium plates with a thickness of 1 mm were applied. It is worth to mention, that the ballistic velocity limit depends on an incident angle of the impactor impact.

✉ Zdzisław Nowak
znowak@ippt.pan.pl

✉ Zbigniew L. Kowalewski
zkowalew@ippt.pan.pl

Tadeusz Szymczak
tadeusz.szymczak@its.waw.pl

[1] Department of Theory of Continuous Media and Nanostructures, Institute of Fundamental Technological Research, Polish Academy of Sciences, A. Pawińskiego 5B, 02-106 Warsaw, Poland

[2] Department of Experimental Mechanics, Institute of Fundamental Technological Research, Polish Academy of Sciences, A. Pawińskiego 5B, 02-106 Warsaw, Poland

[3] Vehicle Type-Approval & Testing Department, Motor Transport Institute, Jagiellońska 80, 03-301 Warsaw, Poland

Moreover, one can indicate that many different effects can be included in numerical simulations of the impact tests. At present, there are plenty publications showing a reasonable accuracy of numerical simulations, especially FEM, when predicting a low, medium and high velocity impact resistance of metal targets. Some representative achievements obtained using different fracture models can be found in [3, 4]. In general, numerically predicted perforation results are restricted by material behaviour description. Therefore, to increase the numerical simulation accuracy it is necessary to understand properly deformation mechanics of materials and formulate a reasonable identified constitutive model. It is common to describe material yielding and material failure separately using a yield criterion with a flow rule for the plastic deformation and fracture criterion. The most popular are the Johnson–Cook (JC) yield criterion with an associated flow rule, and Johnson–Cook fracture criterion (JC-f) uncoupled in the sense of damage influence onto the material elastic and plastic properties. Penetration and perforation of metal targets can proceed through plugging, petalling, ductile hole enlargement and other mechanisms acting either separately or simultaneously depending on the impact conditions. A dependence of the fracture criteria in numerical simulations of high velocity impact on both the stress triaxiality/pressure and Lode angle have been studied by [5]. All these studies showed, that the FE simulations of high velocity perforation with both triaxiality and Lode angle dependent fracture criteria better match the experimental data than those obtained with the use of JC fracture criterion, which includes the effect of stress triaxiality only in terms of stress state problem. In this research, the simulations were carried out using the JC-f fracture criterion reflecting the stress triaxiality and also by the constant ductile Lode angle dependent or independent fracture strain criterion to describe the AM60 target-plate magnesium alloy properties. Finally, the numerically calculated impact resistance and fracture patterns of the target-plates were compared to those in the experiments captured.

Several studies regarding strain-rate dependence of flow stress of magnesium single crystal, polycrystalline magnesium, and magnesium alloy at room and high temperature have been published over the last decade (e.g [6, 7]). Comparative studies concerning the structure and properties of AM60 have been presented by [6, 8, 9]. Compressive deformation behaviour and microstructure evolution of magnesium alloy under quasi-static and dynamic loading have been studied by [7, 10, 11]. The rate dependencies of the flow stress of magnesium and magnesium alloys at strain rates ranging from 10^{-3} 1/s to 10^{2}–10^{3} 1/s are summarized by [12]. These results demonstrate the sensitivity of mechanical strength and rate-dependent behaviour of magnesium to varying texture. A petalling effect appears as a failure mode during impact perforation process, if the hemispherical or conical-nose impactors are applied [13]. It has been found, that failure mode depends strongly on the impact velocity [14]. Petalling can be replaced by the crack opening failure mode, if the impact velocity takes the values close to the ballistic limit. Rusinek et al. [14] have been shown, that in the specimens impacted by the impactor with a relatively low values of the impact velocity no external cracks appeared.

A similar case will be taken into account in this paper, however, for other material and testing conditions. The motivation of current experimental program and numerical simulations is driven by the critical need for data and effective material model that would be able to describe a commercial polycrystalline magnesium alloy behaviour at low loading rates and room temperature. These data may provide a better understanding of the dominant deformation and fracture mechanisms in magnesium alloy under such perforation loading conditions. To conduct dynamic tests, the conical-nose impactor was applied to execute impact onto the stationary disc-shape target plate. The low velocity impact resistance of the material in question was evaluated with the use of dedicated impact tower. It was controlled by computer with dedicated software. The results were expressed by variations of impact energy, impactor velocity, force, and specimen deflection versus time. A wider description of the experimental program is given in Sect. 2. This paper presents an experimental and numerical study of the effects of low velocity impacts (from 7 to 16 m/s) in the AM60 magnesium alloy plates tested at room temperature. Impact responses were numerically investigated using ABAQUS/Explicit Finite Element program [15]. The impact resistance of AM60 was determined under a wide range of energy levels. The results achieved enabled to create a database for identification of the material parameters in models for numerical analysis of the perforation process.

2 Problem description, materials and modelling

2.1 Problem description-perforation of disc plate

Details of the experimental procedure have been already presented by [16]. The samples used for perforation tests were a disc-shape type of diameter and thickness equal to 95 mm and 10 mm, respectively. They were screwed and clamped to the support before each test. The plates were fully clamped by two M10 bolts between two thick circular steel plates with an internal hole (Fig. 1b, c). The bolts compressed specimen and restricted its radial displacement between the supports. The supporting plates were fixed to a strong structural base to prevent against any movement. The impactor had conical-nose shape. All tests were carried out at room temperature using the 9250 HV Dynatup Instron

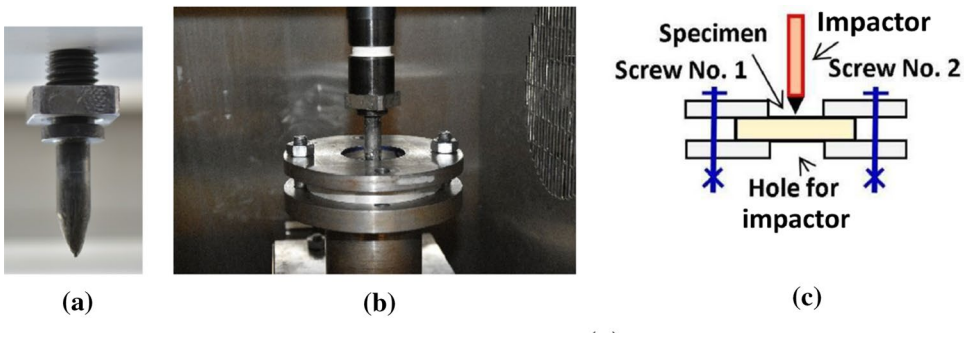

Fig. 1 Details of the loading chain of testing stand: **a** general view of the impactor; **b** specimen mounted in the machine grips; **c** scheme of impact of the target-plate

impact tower. The influence of initial temperature was not studied in detail, mainly due to the complex experimental devices required for highly instrumented tests. Considering the low velocity impact and short-term nature of thermal softening, this article temporarily ignores an impact of the thermal softening. The impact energy capacity for the station is within the range 0–900 J. Sensors of the testing machine enabled measurement of the accumulated energy, force, impactor velocity and penetration versus time.

During an impact, the resistive force acting on the target-plate by the impactor was measured by the loading cell as a function of time. The time histories of the displacement, U_{imp}, and velocity, $V_{\text{imp}}(t)$, were calculated from the measured force-time data by successive numerical integrations software of the Instron impact tower using the following relationships:

$$V_{\text{imp}}(t) = V_{\text{i}} - \int_0^t \frac{F(t) - m_{\text{imp}} \cdot g}{m_{\text{imp}}} \, \mathrm{d}t \tag{1}$$

$$U_{\text{imp}} = \int_0^t V_{\text{imp}}(t) \, \mathrm{d}t \tag{2}$$

where m_{imp} is the mass of impactor, V_{i} is the initial impact velocity of the impactor during perforation and g is the gravity.

Different velocities obtained for the same supporting conditions and impactor were used in assessments of the target-plate perforation. A weight of the dropped mass together with the impactor was constant and equal to 5.77 kg. A radius and angle of the impactor tip were equal to 2 mm and 30 deg, respectively, Fig. 1a. The AM60 plates were examined under four levels of impact energy: 170 J, 260 J, 540 J and 690 J, that corresponded to the impact velocities of impactor in the range of 7 m/s < V_{i} < 16 m/s. After impact tests, the microstructural observations were performed with the use of Olympus PMG3 light microscope and JEOL 6360LA scanning electron microscope. The representative results of the microstructural analysis have been published in the earlier paper by [16] (Fig. 2).

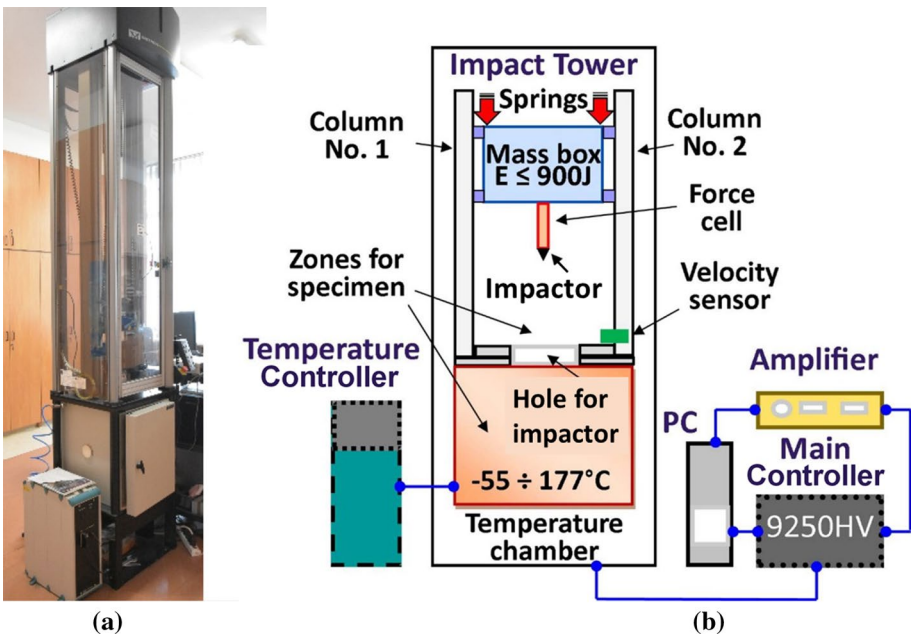

Fig. 2 The 9250HV Dynatup Instron impact tower: **a** general view; **b** scheme showing the main parts of the testing stand

Table 1 Four representative impact tests of AM60 with the conical-nose impactor [16]

Plate material	Impactor material	Impactor velocity (m/s)	Impact energy (J)	Impactor mass (kg)	Response
AM60	Steel	7.72	170	5.77	Penetration stuck
	Steel	9.51	260	5.77	Penetration stuck
	Steel	13.54	540	5.77	Direct penetration
	Steel	15.45	690	5.77	Direct penetration

2.2 The experimental results of the perforation tests

Four representative tests are selected for comparative analysis, and the corresponding impact conditions are listed in Table 1. The experimental results show variation of the accumulated energy, impact force, impactor velocity and impactor displacement depth versus time for AM60 during impact at room temperature for the initial impactor velocity of: 7.72 m/s, 9.51 m/s, 13.59 m/s and 15.45 m/s. The initial impact velocity, V_i , and the residual impact velocity, V_r, were recorded using the Instron software. An analysis of the force variations enabled determination of the accumulated energy and impactor velocity ranges necessary for the impact effects identification.

In Fig. 3a, b the experimental results of impact force and impactor velocity variations versus time are presented for all impact velocity values used for numerical simulations in this research. On the diagrams showing impact force variation two maxima can be easily distinguished. For the lowest impact velocity, $V_i = 7.72$ m/s, they take almost identical value, while for the highest one, $V_i = 15.45$ m/s, the second maximum is significantly greater. The impactor velocity deceleration curves presented as a function of time in Fig. 3b show that for the higher impact velocity its shapes differ essentially in comparison to those obtained for the lower impact velocity levels considered. This demonstrates that the target-plate can stop the mass of impactor, when impact velocity is smaller than $V_i = 9.51$ m/s (or the impact energy is at least 260 J). It should be emphasised, that in the entire research program the impactor remained undeformed plastically and did not exhibit any damage after the impact.

In Fig. 4a, b the experimentally measured impactor displacement and accumulated energy versus time [ms] are presented for all impact velocity values considered in numerical simulations. It has to be noted, that a displacement of the impactor tail was only measured when the tip started to penetrate the plate. It was equal to the crater depth, since the impactor nose erosion was assumed to be negligible small, and, therefore, could be ignored. For the impact velocity of $V_i = 9.51$ m/s only the impactor nose just penetrates entire thickness of the target plate, and as a consequence, the plate becomes to be partially perforated. Variation of the accumulated energy versus time are presented in Fig. 4b. Depending on the impact velocity a time to achieve the full perforation of the AM60 plate with thickness of 10 mm may differ significantly. For the impact velocity of $V_i = 13.59$ m/s and $V_i = 15.45$ m/s the accumulated energy reached the maximum value after $t = 2.0$ ms and 2.5 ms, respectively, and it was fixed on this level later during perforation process.

To study an impact performance of the AM60 plate under different impact velocity values (impact energy values), the comparisons of impact force–displacement curves are presented in Fig. 5.

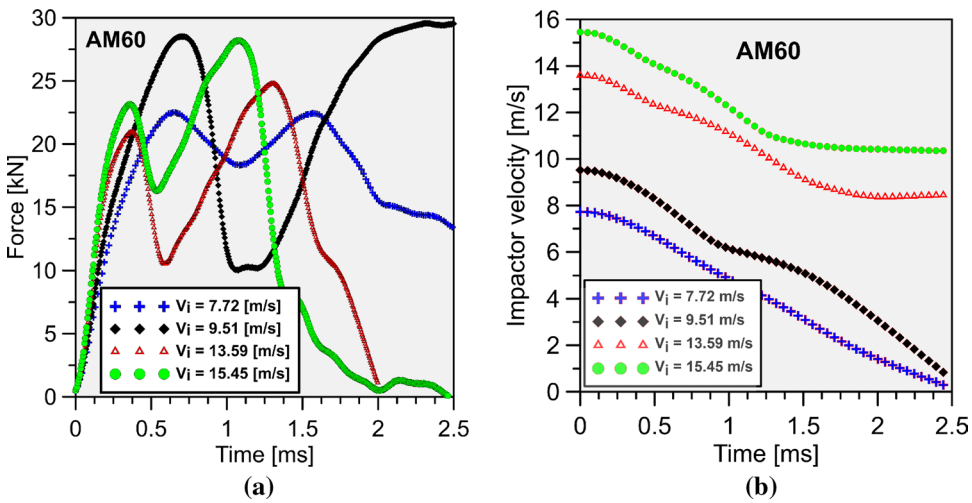

Fig. 3 Variation of the impact force and impactor velocity versus time for the AM60 during impact at room temperature

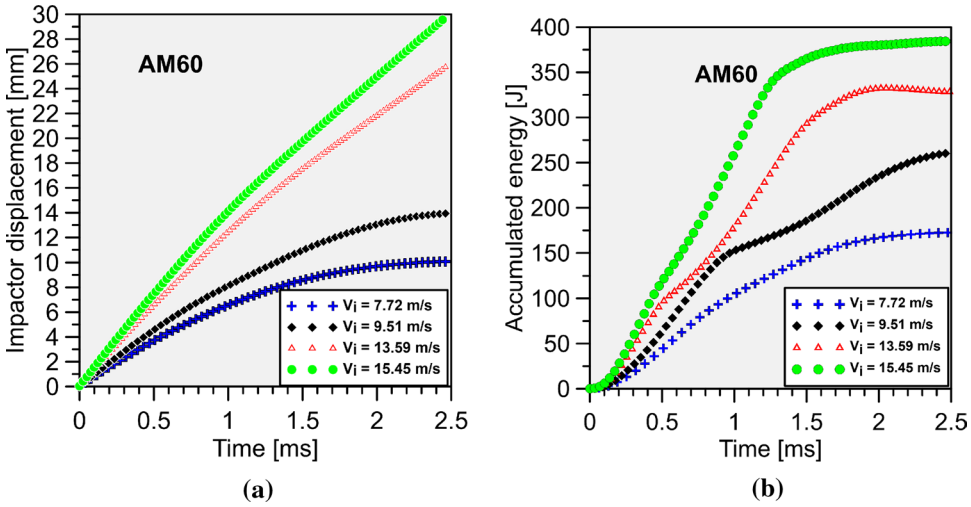

Fig. 4 Impactor displacement and accumulated energy versus time (ms) during low impact perforation for the AM60 alloy at room temperature

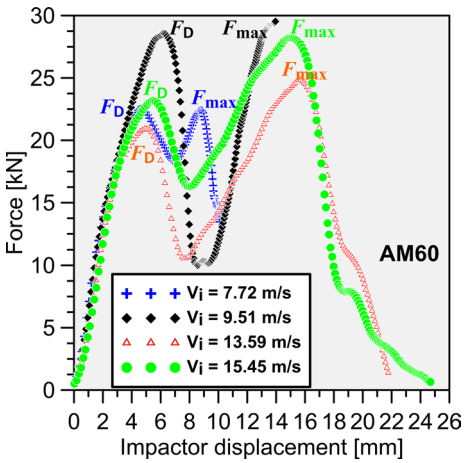

Fig. 5 Impact force–displacement curves during low velocity impact tests for the AM60 target-plate impacted under impact energy of 170 J (V_i = 7.72 m/s), 260 J (V_i = 9.51 m/s), 540 J (V_i = 13.59 m/s), 690 J (V_i = 15.45 m/s)

The perforation of a plate represents a sequential process. In case of the perforation of thick target-plate with low impact velocities the plate thickness is separated into the region that experiences ductile hole growth and region that fails by discing or plugging failure modes. The impacted target-plate accumulates damage right from the beginning of the impact process when the ductile hole enlargement takes place. Ductile hole growth occurs by plastic deformation causing material to flow upward from the penetrating impactor, thus accumulating mass on the top of plate and the plate undergoes a bending mode. If the material is sufficiently brittle, like AM60, a portion of the back face may delaminate abruptly, causing discing or dishing/plugging failure. For velocity impact 13.59 and 15.45 m/s, as the impactor traverses the plate a plugging failure is form, causing a section of the remaining material to be rapidly displaced with a very little resistance.

When the conical-nose impactor penetrates the plate, the impact force increased non-linearly until it reached the damage extension threshold F_D. After that, the plate material that flow upward from the impactor, accumulating mass on the top of plate, led to a sudden drop of the impact force. Then, the impact force continued to rise to the peak force F_{max}, because the kinetic energy stored in the impactor still enforced penetration of the plate. When the conical-nose of impactor left the target-plate, the force gradually decreasing.

One can easily indicate, that F_D and F_{max} during the impact with V_i = 7.72 m/s were on the same level of about 22.5 kN. The F_D during the impact with V_i = 9.51 m/s was about 28.75 kN, and F_{max} was around 30 kN. Both these forces for the impact with V_i = 13.59 m/s were 21.25 kN and 26.25 kN, respectively.

The impact force threshold F_D of the impact with V_i = 13.59 m/s was significantly smaller than that of the impact with V_i = 9.51 m/s. The F_D during impact with V_i = 15.45 m/s was also significantly smaller than that of the impact with V_i = 9.51 m/s. This was because a certain part of the impactor passed through the target-plate and there was a damage development in a more unstable form. An analysis of the force variations enables to indicate the accumulated energy range that is responsible for the effect occurrence. One can find it for the impact energy within the range from 170 to 260 J.

Residual velocity of the impactor plays an important role during evaluation of the target material resistance. In Fig. 6, the experimental results representing the residual velocity, V_r, captured using the conical-nose impactor are depicted as a function of the impact velocity V_i. To calculate values of the residual velocity, in case when the plastic deformation of the impactor during impact is negligible small, the Recht–Ipson model with the later numerical approximation

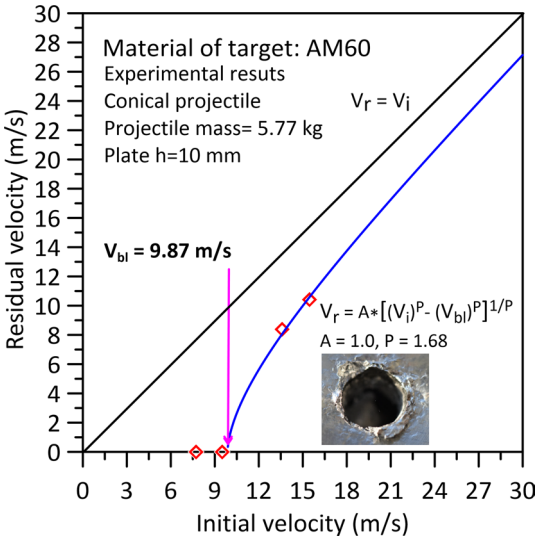

Fig. 6 Residual velocity V_r versus initial velocity V_i for AM60 target-plate

by Lambert was adopted [17, 18]. The model can be expressed by the following formula:

$$V_r = A(V_i^P - V_{bl}^P)^{\left(\frac{1}{P}\right)}. \quad (3)$$

where A and P are the model constants controlling the shape of the residual velocity versus initial velocity curve; V_r is an impactor residual velocity; V_i is an impactor initial velocity; V_{bl} is a ballistic limit velocity. Values of constants A and P were assumed to be within the following ranges $0 \le A \le 1$ and $P > 1$, respectively. They were determined through the least square fitting of the residual velocity versus impact velocity relationship established on the basis of tests executed using the conical-nose impactor. For the plate of 10 mm thickness and conical-nose steel impactor of 12 mm diameter the best fitting values were as follows: $A = 1.0$, $P = 1.68$. As it is clearly seen in Fig. 6, for the range of impact velocities taken into account, the V_r–V_i curve remains quite far from the characteristic corresponding to the condition represented by $V_r = V_i$. For the AM60 target-plate tested, the ballistic limit was found to be $V_{bl} = 9.87$ m/s.

The observed fracture patterns were characterized by a ductile hole enlargement (Fig. 7a1, b1) and radial fracture at rear side in the form of short petals (Fig. 7a2, b2). One can also indicate some shear fracture of petals identified on specimens recovered after tests. A similar fracture patterns were obtained by [19] for TRIP 1000 steel sheets subjected to low velocity perforation by conical-nose impactors. From Fig. 7a, b one can also find that the hole perforated in the target-plate is cylindrical. Its rear side diameter is not much larger than that of the front side obtained. This is due to the rear side fracture caused by the radial oriented damage mentioned above.

The effect of friction was evaluated using the steel–steel results previously reported by [14, 19]. According to [14] two friction conditions should be considered: lubricated case ($\mu \approx 0$) and dry ($\mu > 0$). Taking into account the lubricated condition, several layers of grease and teflon were applied in the impactor/plate interface. The impactor in our research was not lubricated in all tests. As it was concluded in the paper of [19] and confirmed in [20, 21], the failure mode of the plates for low impact velocities was not affected by the friction condition applied. Based on the results of papers

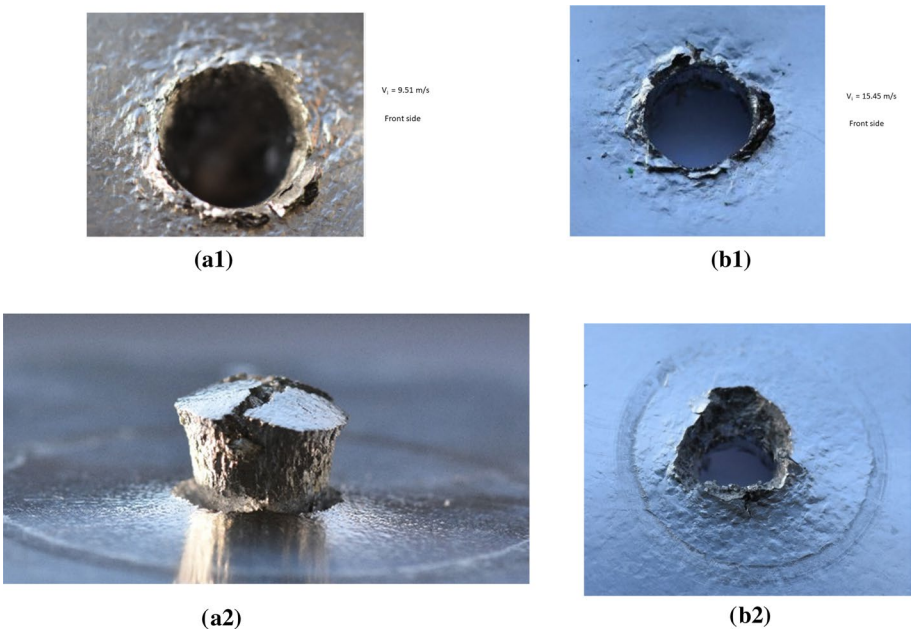

Fig. 7 The hole perforated in the target-plate for the AM60 during impact at room temperature with the initial impactor velocity of 9.51 m/s and 15.45 m/s (front (**a1**, **b1**) and rear (**a2**, **b2**) side views)

discussed above, the friction coefficient was assumed to be $\mu = 0.10$ for the low velocity impacts with conical-nose impactor. Additionally, it has to be emphasised, that constancy of the friction coefficient is based on the assumption of a constant pressure along the impactor/target-plate interface for the impact velocities and conical-nose impactor of mass 5.77 kg studied. In our impact simulations for the conical-nose steel rods perforating AM60 plates with impact velocity 7.72, 9.51, 13.59 and 15.45 m/s, we compared predictions with $\mu = 0$, 0.05, 0.10 and 0.30 to penetration experimental data (impact force, velocity, energy and displacement). Model predictions for impact velocities considered agree well with penetration experimental data only with $\mu = 0.10$.

2.3 Sample material-AM60 magnesium alloy

As it was mentioned earlier, the commercial die-cast polycrystalline AM60 magnesium alloy was chosen for tests. Details of the casting procedure can be found elsewhere [22].

Selected chemical, mechanical and physical properties of the material are presented in Tables 2, 3 and 4, respectively. AM series of magnesium alloys (AM50, AM60, AM60B) are well suited for applications requiring a high elongation and toughness. The response of magnesium alloys samples into quasi-static or dynamic compression and tension have been widely reported in the available literature. Compressive properties of three die-cast magnesium alloys (AM20, AM50, and AM60) have been investigated at a nominal strain rate range from 0.001 s^{-1} to approximately 1700 s^{-1} by [23]. The high strain rate experiments were conducted using a Split Hopkinson Bar apparatus. At strain rates above 1500 s^{-1} there was substantially higher work hardening and strain rate sensitivity compared with that observed for the quasi-static tests at the low strain rates. [24] investigate the mechanical behaviour and the operative deformation mechanisms of die-cast AZ91 and AM60 alloys at impact strain rates under a wide range of temperatures in tension and compression. [25, 26] studied also influence of strain rate and stress state on the mechanical behaviour of die-casting AM60. The test results showed that the yield stress of such material increases slightly with the strain rate at uniaxial tension. It was verified that AM series of alloys follow the von Mises yield criterion, with nearly symmetrical yielding behaviour between uniaxial tension and compression at the same level of strain rates. Moreover, it was shown that the equivalent fracture strain or effective ultimate strength at uniaxial tension and shear states were relatively close to each other, however, significantly smaller than those at compression. The effect of strain rate on tensile properties of die-cast AM60B and AM50A test bars at room temperature is reported by [27]. The results of [27] are discussed in terms of the work hardening characteristics, strain rate sensitivities of the materials, and parameters of the Johnson–Cook model. It has been found, that the flow stress increases while the elongation is not affected by strain rates within the range from 15 to 130 s^{-1} and the energy absorption during deformation increases emphasizing the positive properties of magnesium die-cast alloys for safety related applications. The energy absorption of High Pressure Die Cast (HPDC) magnesium alloys AM20, AM50, AM60, AZ91 and the aluminium alloy AlSi7Mg was investigated by [28]. For AM60 alloy, single plates cast with different thickness were tested to investigate the effect of plate thickness on the shear-bolt mechanism. The paper by [29] presents experimental study, including the test method and the data analysis, for the die-casting AM60B. Uniaxial tension tests were carried out at various strain rates from 5×10^{-4} to $1 \times 10^{+2}$ s^{-1}. Uniaxial compression and shear tests at strain rates from 5×10^{-4} to 5×10^{-2} s^{-1} were also carried out. All the specimens were cut off from die-casting plates of AM60B with thickness of 2.6 mm. The results showed, that the yield stress of AM60B increased slightly with the strain rate at uniaxial tension. However, this tendency was not very clear due to the relatively large scatter in the results captured. The results of papers discussed above establish the fact, that the quasi-static and dynamic stress–strain curves for AM60B show a similar shape as for AM60 and indicate, that similar quasi-static and dynamic mechanical properties conclusions have to be drawn for all Mg–6Al–0.3Mn-type alloys (e.g. AM60). The tensile and quasi-static compressive curves of AM60 are illustrated in Fig. 8a adopted from [16, 23, 24, 30]. The dynamic experimental data for AM60 alloy is taken from papers [23–26] and are reported in Fig. 8b. For AM60 alloy used in this study, however, the tensile-compressive asymmetry at various strain rates is small, so the tensile yield stress is used both for tension and compression conditions. The results presented in Fig. 8a, b are used in the numerical simulations of the impact low-velocity perforation, that are discussed in the next section.

2.4 Material of impactor

The 12-mm diameter impactor was fabricated using tool steel of hardness equal to 207HB. The impactor was additionally loaded by a special additional mass to obtain 670 J impact energy under initial velocity of 15.45 m/s. The mechanical properties of the impactor material were as follows: Young's modulus $E = 210$ GPa, density 7850 kg/m^3 and Poisson's ratio $\nu = 0.3$.

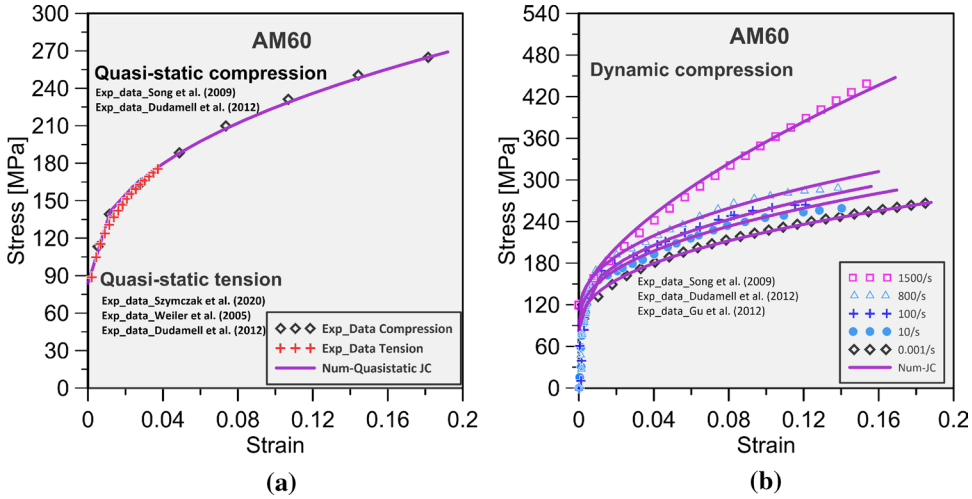

Fig. 8 Quasi-static tensile and compressive (**a**); and dynamic compressive (**b**) stress–strain characteristics of the AM60 at room temperature

Table 2 Chemical composition of AM60 (wt%), [31]

Mn	P	Si	Ni	Fe	Ca	Al	Zn	Th	Mg
0.31	0.004	0.022	0.002	0.012	0.0005	6.14	0.3	0.06	93.4

Table 3 Selected mechanical properties of AM60, [32]

Material	Elastic modulus (GPa)	Shear modulus (GPa)	Poisson's ratio	Yield stress (MPa)
AM60	45.7	17.3	0.34	98

Table 4 Selected physical properties of AM60 [31, 33]

Material	Density (kg/m^3)	Specific heat (J/g K)	Thermal conductivity (W/m K)	Melting point (Celsius scale)
AM60	1740	1.02	61	575

3 Constitutive modelling

3.1 Target-plate of AM60

In this study the elastic deformation was described by the Hooke's law,

$$\boldsymbol{\sigma} = 2G\boldsymbol{\varepsilon} + \lambda(\boldsymbol{\varepsilon}), \tag{4}$$

where $G = E/2(1+\nu)$—Kirchhoff's modulus, $\lambda = E\nu/(1+\nu)(1-2\nu)$—Lame parameter, E denotes the Young's modulus and ν is the Poisson's ratio.

To describe the inelastic behaviour, the additive elastic/plastic decomposition of strain rate tensor was used:

$$\dot{\boldsymbol{\varepsilon}} = \dot{\boldsymbol{\varepsilon}}^{e} + \dot{\boldsymbol{\varepsilon}}^{\mathrm{pl}}. \tag{5}$$

The plastic part of deformation was described by the associated flow rule:

$$\dot{\boldsymbol{\varepsilon}}^{\mathrm{pl}} = \dot{\lambda}\,\frac{\partial H}{\partial \boldsymbol{\sigma}}, \tag{6}$$

where the plastic potential function H was taken to be equivalent to the yield function, and $\dot{\lambda}$ is the unknown multiplier (so-called consistency parameter). Taking this into account led to the following formula,

$$\dot{\boldsymbol{\sigma}} = \boldsymbol{D}^{e} : \left(\dot{\boldsymbol{\varepsilon}} - \dot{\boldsymbol{\varepsilon}}^{\mathrm{pl}}\right), \tag{7}$$

where the equivalent strain was calculated from the equation $\boldsymbol{\sigma} : \dot{\boldsymbol{\varepsilon}}^{\mathrm{pl}} = \sigma_Y^T\,\dot{\bar{\varepsilon}}^{\mathrm{pl}}$ [34].

The Huber–Mises–Hencky (HMH) yield criterion was expressed by the following formula:

$$F^{\mathrm{HMH}} \doteq \overline{\sigma} - \sigma_Y^T = 0, \tag{8}$$

where σ_Y^T is the yield stress in tension of the AM60, $\overline{\sigma} \doteq \sqrt{3/2\,\boldsymbol{s} : \boldsymbol{s}}$ represents the equivalent stress and $\boldsymbol{s}$ is the deviatoric stress tensor.

The inelastic behaviour of AM60 was modelled using the JC constitutive relation. It captures effects of strain hardening, strain-rate hardening and thermal softening on the yield stress [35].

In the JC model [35], the yield stress in Eq. (8) can be expressed in the following way:

$$\sigma_Y^T(\bar{\varepsilon}^{\mathrm{pl}}, \dot{\bar{\varepsilon}}^{\mathrm{pl}}, T) \doteq \left[A + B\,(\bar{\varepsilon}^{\mathrm{pl}})^{n}\right]\left[1 + C\,\ln\left(\frac{\dot{\bar{\varepsilon}}^{\mathrm{pl}}}{\dot{\varepsilon}_0}\right)\right]\left[1 - (T^{*})^{m}\right], \tag{9}$$

where $\bar{\varepsilon}^{\mathrm{pl}}$ denotes the equivalent plastic strain, while its rate can be defined as:

$$\dot{\bar{\varepsilon}}^{\mathrm{pl}} = \dot{\varepsilon}_0 \exp\left[\frac{1}{C}(R-1)\right], \qquad \text{for} \qquad \dot{\bar{\varepsilon}}^{\mathrm{pl}} > \dot{\varepsilon}_0, \tag{10}$$

and $\dot{\varepsilon}_0$ is the reference strain rate (0.001 s^{-1} in this work). The rest parameters in Eq. (9) are: A—the initial yield stress under the reference temperature T_{Ref} and strain rate of $\dot{\varepsilon}_0$, B and n—the strain hardening coefficient and the exponent, respectively, C—strain rate hardening, m—parameter reflecting thermal softening effects, $R = R(\bar{\varepsilon}^{\mathrm{pl}})$—the ratio of the yield stress for strain rate greater than 0 to the static yield stress, and $T^* = (T - T_{\mathrm{Ref}})/(T_{\mathrm{m}} - T_{\mathrm{Ref}})$, where T_{m} is the melting temperature (575 °C in this work) and T_{Ref} is the reference temperature (20 °C).

The JC equation was used to study the effects of low velocity impacts on the AM60 target-plates at room temperature. Material can be heated up by the impact energy dissipation. The heat is generated at the contact surface between the impactor and the target plate, which increases the temperature of the contact surface between the impactor and the target. At the same time, the heat will be conducted to the impactor and target plate. Because the specific heat of the AM60 alloy plate material, $C_{\mathrm{p}} = 1020$ J/kgK, is high and the thermal conductivity of AM60 alloy, 61 W/(m K), is small, the area where the heated temperature rises is relatively small, and the amount of heat dissipated is limited. In case of the low velocity impact of AM60 alloy and short-term nature of thermal softening, this article temporarily ignores the thermal softening in the analysis and the yield stress in Eq. (9) of the JC model at room temperature can be express by a function of strain and strain rate, in the following way:

$$\sigma_Y^T(\bar{\varepsilon}^{\mathrm{pl}}, \dot{\bar{\varepsilon}}^{\mathrm{pl}}) \doteq \left[A + B\,(\bar{\varepsilon}^{\mathrm{pl}})^n\right]\left[1 + C\,\ln\left(\frac{\dot{\bar{\varepsilon}}^{\mathrm{pl}}}{\dot{\varepsilon}_0}\right)\right]. \tag{11}$$

In this paper, the least-squares method was employed to calibrate the model parameters (A, B, n, and C), shown in Eq. (11). The mean squared error was calculated for N number of data points which represents the true stress obtained from the experimental tests, and the true stress predicted by the constitutive model. The model parameters A, B, and n could be identified by adopting the stress–strain data from the quasi-static tensile tests, Fig. 8a. The results of tests shown in Fig. 8b indicate, that AM60 is strain rate sensitive to some extent. The JC constitutive relation defined in Eq. (11) which includes the linear elasticity, von Mises yield criterion, associated flow rule, isotropic strain hardening, and strain-rate hardening, was calibrated for AM60 using the experimental data adopted from [16, 23–26, 28, 29]. Parameter C represents the strain rate sensitivity coefficient, which could be calibrated using the stress–strain data corresponding to the four different strain rates considered in this study, Fig. 8b. The curve fitting parameters (A, B, n, and C) are listed in Table 5 and the fitting curves are presented in Fig. 8a, b. Note, that the parameter values for AM60 differ a bit from those presented in previous papers, e.g. [27]. This is due to the slightly different calibration method used in this study. Subsequently, the curves with the calibrated JC model were compared with the experimental results to estimate and accept the accuracy of JC model characterizing the stress-strain relationship of AM60. Details regarding the calibration procedure can be found in [36, 37].

To simulate the perforation process a fracture criterion must be considered. The details of material fracture during punching processes have been a subject of debate in the past. Phenomenological models incorporating Lode effect have been widely studied, e.g. [38–40].

Among papers which are devoted to facture prediction capability of the magnesium alloys, reflecting simultaneously the stress triaxiality and Lode angle, one can recommend the article of [38]. The Authors showed a good capability for facture prediction of AZ31B-H24 magnesium alloy at room temperature.

Torki et al. [41] have been found, that the strain to failure for ductile metals is rather weakly dependent on the Lode parameter for shear-dominated loadings. In opposite to that, it is strongly dependent in the case of tension or compression. In conclusion it could be stated, that the Lode angle parameter plays important role at the finite deformation or late stage of deformation prior to fracture of magnesium alloys. However, this issue still needs efforts to provide better justification of the current knowledge.

In the present study, the strain, stress triaxiality, and Lode parameter effect were considered in the same way as that in ABAQUS used. The fracture criterion for ductile material was taken with or without Lode dependence. The strain, stress triaxiality and strain rate were used in the fracture criterion, called JC-f. It was assumed, that a damage initiates if the effective plastic strain, $\bar{\varepsilon}_{\mathrm{f}}$, exceeds a critical value. There is no distinction between the tensile and compressive states of a material point in this criterion. Ductile fracture strain was identified in numerical simulations to fit the experimental data concerning the impact force history.

During the perforation process a stress state was described by the stress triaxiality and Lode angle parameter. The stress triaxiality was defined as the ratio of the mean stress and von Mises stress. The Lode angle parameter was used to traced a ratio of the third and second deviatoric stress tensor invariants. It varies between −1 (axisymmetric compression) and 1 (axisymmetric tension). The ductile fracture strain criterion with or without the Lode-dependent and Lode-independent JC-f fracture model were implemented in ABAQUS FE program. In

the ductile fracture strain criterion and JC-f criterion, the failure of a material point was calculated based on the effective plastic strain.

The equivalent fracture strain, $\bar{\epsilon}_f$, is greatly dependent on the stress triaxiality, η, Lode angle parameter, $\bar{\theta}$, and the equivalent strain rate, $\dot{\bar{\epsilon}}$, for most metallic materials. In the plasticity of magnesium alloys the fracture criterion representing this relationship at room temperature can be expressed by

$$\bar{\epsilon}_f = f(\eta, \bar{\theta}, \dot{\bar{\epsilon}}) \tag{12}$$

with

$$\bar{\theta} = 1 - \frac{2}{\pi}\arccos(\xi) \tag{13}$$

where ξ is the third deviatoric stress invariant J_3 normalized by equivalent stress, $\bar{\sigma}$ and it reads

$$\xi = \frac{27}{2}\frac{J_3}{\bar{\sigma}^3} \tag{14}$$

A fracture mechanism for AM60B has been studied by [29]. The results are presented in Fig. 9. As the Authors indicated, there is no obvious relationship between the fracture strain and strain rate at uniaxial tension and compression. For shear, the fracture strain decreases with higher strain rate.

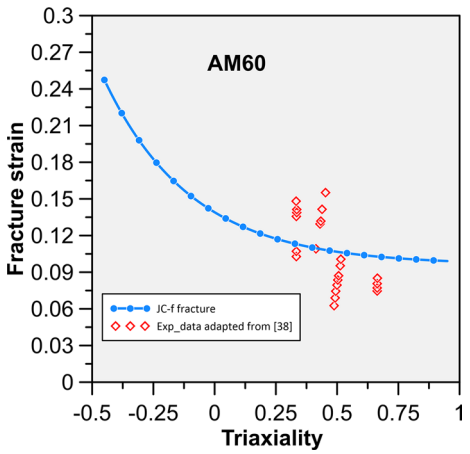

Fig. 9 Fracture strain versus triaxiality characteristic of AM60 at room temperature used in FE analysis. Experimental data points adapted from [29]

On the basis of deformation process observations [29], quasi-static and dynamic mechanical properties for AM type magnesium alloys presented in Sect. 2.3, and the impact force history, it is reasonable to assume $\bar{\epsilon}_f = 0.10$ for AM60.

When ignoring the effect of Lode angle parameter, the Lode angle independent JC-f fracture criterion [35] with temperature term is widely adopted in practical engineering. In JC-f fracture model the equivalent plastic strain at the damage onset, $\bar{\epsilon}_f$, can be given by

$$\bar{\epsilon}_f = [D_1 + D_2\ \exp(D_3\eta)][1 + D_4 \ln\left(\frac{\dot{\bar{\epsilon}}^{pl}}{\dot{\epsilon}_0}\right)](1 + D_5 T^*) \tag{15}$$

where $\eta = p/\bar{\sigma}$, denotes stress triaxiality with p and $\bar{\sigma}$ representing hydrostatic pressure, and equivalent von Mises stress, respectively, and D_1 through D_5 are material parameters. Equation (15) reflects effect of triaxiality and thermal softening if $D_5 \neq 0$. In case of the low velocity impact at room temperature it was assumed that thermal softening can be neglected and the impact should not be treated as adiabatic. The JC fracture criterion defined in Eq. (15) was calibrated for AM60 using data from [10, 11, 29]. The parameters for the isotropic strain hardening, strain-rate hardening and triaxilality included in the JC-f criterion were calibrated separately in the same manner as for the constitutive relation. The stress triaxiality parameters (D1, D2 and D3) were determined using the quasi-static tensile tests. The strain rate parameter D4 was determined on the basis of dynamic tensile tests. If D5 = 0 in Eq. (15), then the problem becomes to be temperature-independent (for low velocity impact tests at room temperatures). A set of the following material constants were taken into account in the JC-f criterion: $D_1 = 0.0575$, $D_2 = 0.0257$, $D_3 = -2.7978$, $D_4 = 0.0972$, $D_5 = 0$. The curve of $\bar{\epsilon}_f$ versus stress triaxiality η is presented in Fig. 9. It was assumed that damage started to develop, if:

$$\sum \frac{\Delta\bar{\epsilon}^{pl}}{\bar{\epsilon}_f} = D_f \tag{16}$$

Table 5 Model parameters for AM60

Material	Yield stress	Strain hardening	Exponent	Strain rate hardening	Temperature softening	
	A (MPa)	B (MPa)	n	C	m	
AM60	95	405.72	0.469	0.0148	0.0	
Fracture strain	D1	D2	D3	D4	D5	D_f
AM60	0.1986	0.1518	− 3.311	− 0.015	0.0	1.0

where $\bar{\varepsilon}_f$ is the equivalent fracture strain.

Damage was initiated in numerical calculations, when Eq. (16) was satisfied and the stress components were set to zero level at the integration point. The material point was assumed to be failed if, the Eq. (16) was fulfilled at all integration points of the element. In such a case the element was removed either from the mesh or domain considered.

The constitutive relation and fracture criterion were calibrated by minimising the sum of squares between the model results and corresponding experimental data [36, 37]. The melting temperature of the materials was taken as $T_m = 848$ K, while the room temperature as $T_0 = 293$ K. The user-defined reference strain rate was taken as $\dot{\bar{\varepsilon}} = 0.001\ s^{-1}$.

To describe the initiation and propagation of the perforation in finite element calculations, a damage indicator needs to be refined. In the present paper, the non-linear power law of damage accumulation was adopted. A damage indicator D was defined.

In numerical analysis to be presented in Sect. 4 two damage models will be used within ABAQUS software, i.e. ductile damage model with and without Lode dependence and JC-f model.

3.2 Details of the numerical analysis

A diagram of the impact force versus time $F(t)$ can be determined using a time dependent deceleration of the impactor $a(t)$ during perforation [20], expressed by:

$$F(t) = m_{\text{impactor}} \times (a(t) + g) \tag{17}$$

where g is the gravity.

Numerically calculated model of the impactor and experimental setup applied in simulations are presented in Fig. 10a–c.

Figure 10c shows the boundary conditions for the target-plate (specimen), supporting plates and impactor. The specimen was located as a free body between two supporting plates with central holes. The top supporting plate was compressed by uniformly distributed forces. For bottom supporting plate a displacement in the impact direction was fixed. The rigid cylindrical impactor with conical-nose shape impacted vertically the specimen plate with an initial velocity of V_0.

Isotropic analysis of 3D deformations of the target-plate was carried out at room temperature. The target-plate domain was discretized using ten-node (C3D10M) modified quadratic tetrahedron finite elements (ABAQUS element

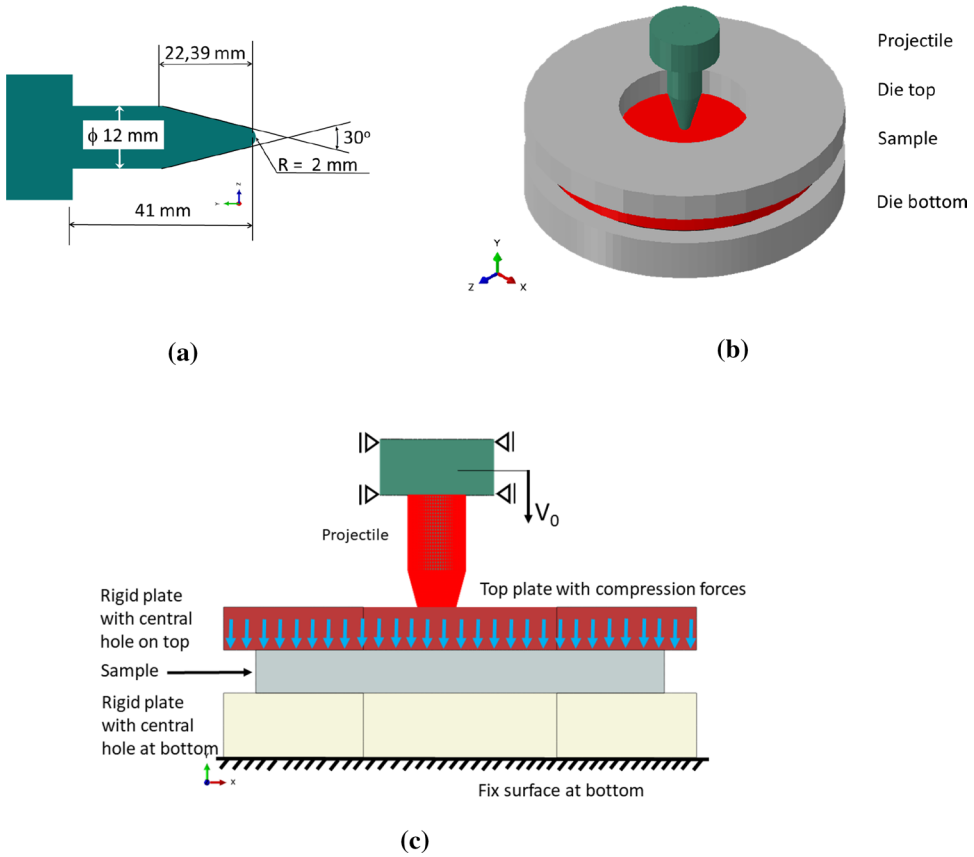

Fig. 10 Details of the experimental setup in simulations: **a** impactor geometry and its main dimensions; **b** main elements of the stand; **c** boundary conditions for the target-plate (specimen), supporting plates and impactor

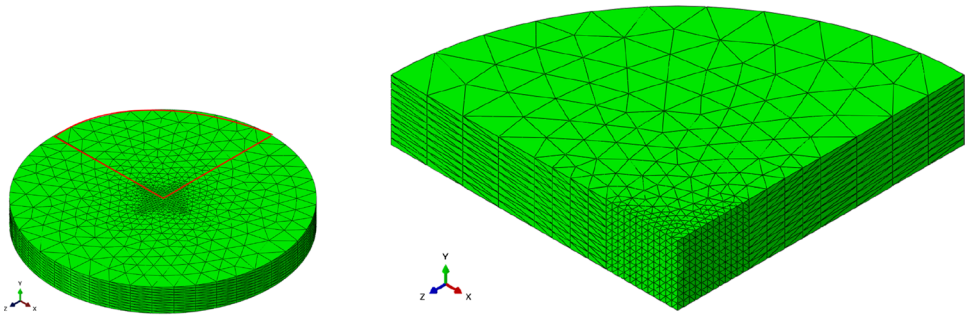

Fig. 11 The target-plate mesh used in the numerical simulations: **a** total view; and **b** magnified view of the quarter part of it that was taken for calculations

library). The full region of 10 mm radius of the target-plate was discretized by finite elements of the following sizes 0.2 mm × 0.2 mm × 0.2 mm. The element size was gradually increased to 0.8 mm × 0.6 mm × 0.2 mm near the outer edges of the specimen (see Fig. 11). The top and bottom gripping plates as well as the impactor were discretized by means of 4-node 3D bilinear rigid quadrilateral (R3D4) and 3-node 3D rigid triangular facet (R3D3) elements.

There were 24,768 elements in total covering the target-plate. In case of the top and bottom gripping plates their number was equal to 3742. The impactor was discretized using 8090 finite elements. Thus, the total number of elements was equal to 36,600. Figure 11a shows the entire target-plate with element mesh, while Fig. 11b presents a quarter of it with 6192 tetrahedron elements, denoted as C3D10M in ABAQUS notation. Mesh-independent results were enhanced by application of the viscoplastic approach. It led to the well-posed boundary value problem already studied in the past [42–44].

Based on the experimental scheme, the impactor was defined as a rigid body without any erosion on its surface after impact. A constant value of the Coulomb friction coefficient μ was assumed, similarly as other authors usually introducing [1, 20]. An influence of temperature and sliding velocity on the friction coefficient was not taken into account. It has to be emphasised that constancy of the friction coefficient is based on the assumption of a constant pressure along the impactor/target-plate interface. Such simplification was validated for the metallic targets of small thicknesses. In the case considered the same assumption was postulated. The authors confirmed this hypothesis by FE analysis of the pressures change during 10 mm thickness plate perforation carried out for different impact velocities in the range of 5–20 m/s with conical-nose impactor of mass 5.77 kg. The failure criterion applied involved a procedure of damaged elements removing from the mesh under simultaneous assumption of the energy balance. It has to be noted, that during the FE analysis the number of elements deleted was very small, and, therefore, the mass conservation law was acceptably fulfilled. The general contact algorithm in ABAQUS was employed and the dynamic Coulomb's friction coefficient of 0.10 was assumed at the impactor/target-plate interface, as well as the target-plate and gripping-plates interfaces. The work done on the movement of top gripping-plate with compression forces was estimated to be equal around 122.8 mJ/m^2.

4 Results of numerical simulations

FE model for perforation process simulation of the AM60 plates was developed in ABAQUS/Explicit [15]. A fully 3D configuration of the model enabled to describe a dynamic deformation reflecting fracture mode that characterized the perforation of metallic target-plates by the impactor.

4.1 Impact force during perforation

Impact force history during perforation process with ductile fracture criterion is presented in Fig. 12a–d. For a time period less than 0.4 ms, the impact force values were quite close to those in experiments achieved. Moreover, it is clearly shown, that for a time within a time period from 0.7 to 1.0 ms the values of impact force were slightly different than those in the tests observed. The errors in values of impact force as a function of time are quantified on the level of 20%.

4.2 Deformation analysis of the AM60 target-plate

There are several different mechanisms playing a crucial role in the target failure. They may occur singly or in combinations of two or more. For example, [45] identified eight most commonly occurring types of failure of thin or intermediate targets [46, 47].

Deformation process of the specimens in case of low velocity impact perforation can be divided into two parts, i.e. the global deflection and local indentation. The local indentation had a shape of the impactor head. The conical-nose

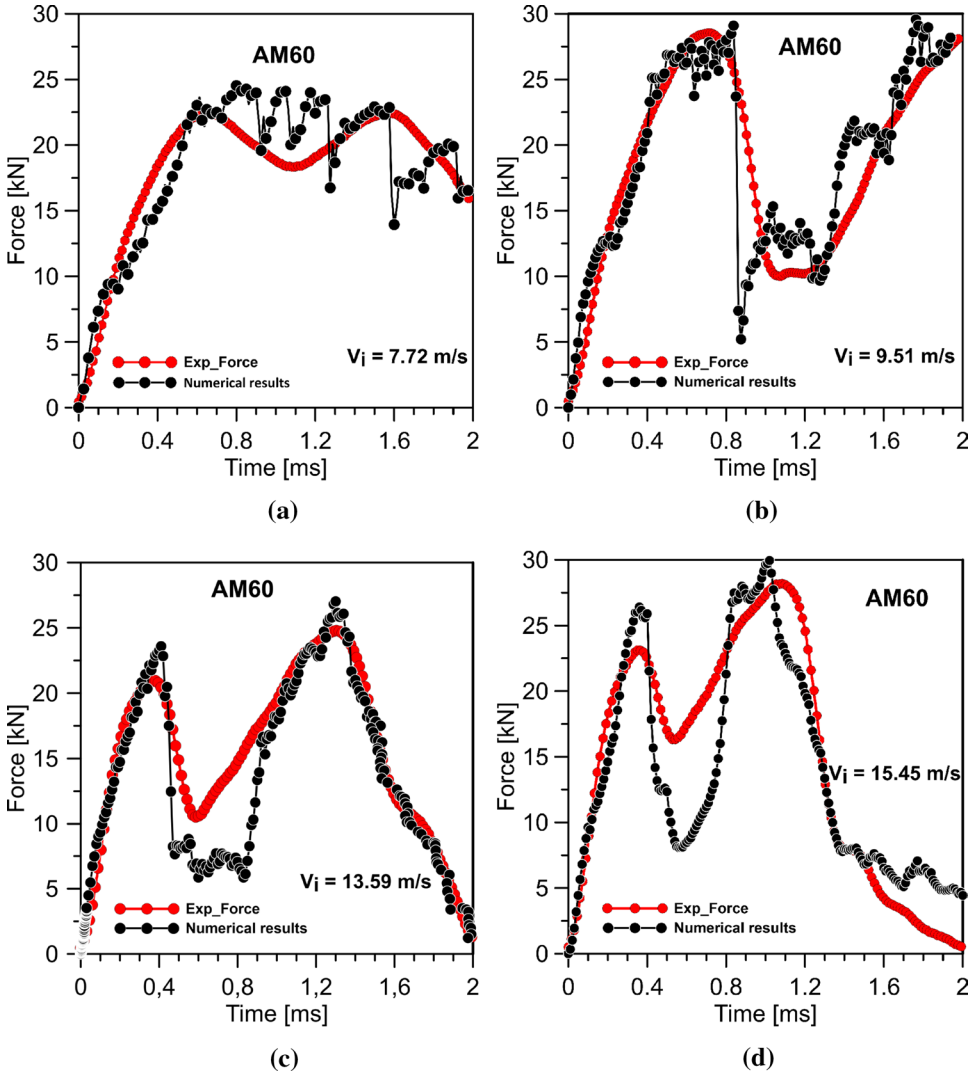

Fig. 12 Numerical model validation: comparison of impact force variations obtained in simulations and experiments for the impact velocity of: **a** V_i = 7.72 m/s; **b** V_i = 9.51 m/s; **c** V_i = 13.59 m/s; and **d** V_i = 15.45 m/s

impactor penetrated the plate causing a ductile hole enlargement leading to the material elongation by the plastic flow of the area below the impactor forming, as a consequence, the circular hole. Since a support of the top and bottom of the plate was kept vertically, the impacted region of the plate was bent and stretched inelastically in the deformed configuration. When the effective plastic strain achieved a relatively high value, the fracture was initiated at the hollow circle of the impacted region. Finally, the fracture process propagated through the plate thickness while the impactor penetrated the plate. It has to be emphasised, that in the case of 5.77 kg mass impacted on the target-plates the inertia effect could be neglected provided that the impact velocity would be low (up to about 20 m/s). Such negligible effect was also demonstrated by [14]. They presented almost the same numerical scheme for low-velocity impact simulations of the mild steel. However, their analysis was carried out for the hemispherical nose shape impactor.

Details of the vertical displacement stages, $U_2 = U_Y$, in the AM60 target-plate after impact are shown in Fig. 13 for the initial impact velocity of the impactor equal to 15.45 m/s.

Since the impactor impacted the target-plate surface, the plate material directly below its nose began to plastically flow radially outwards from the centre (as can be seen in Fig. 13b). As a consequence, a lip of material was created circumferentially around the crater.

Figure 13 illustrates the states of target-plate around the impact zone in different time periods, thus, reflecting a development of the impactor penetration process. For impact velocity of 15.45 m/s at time equal to 0.2 ms; 0.7 ms and 2 ms a depth of penetration attained the length equal to 3.07 mm; 10.29 mm and 25.88 mm, respectively.

Variations of the equivalent plastic strain at three time intervals equal to 0.1 ms; 0.7 ms and 2.0 ms are shown in Fig. 14. As it is clearly seen, the penetration process developed directly after the impactor impacted the target-plate, Fig. 14a, b.

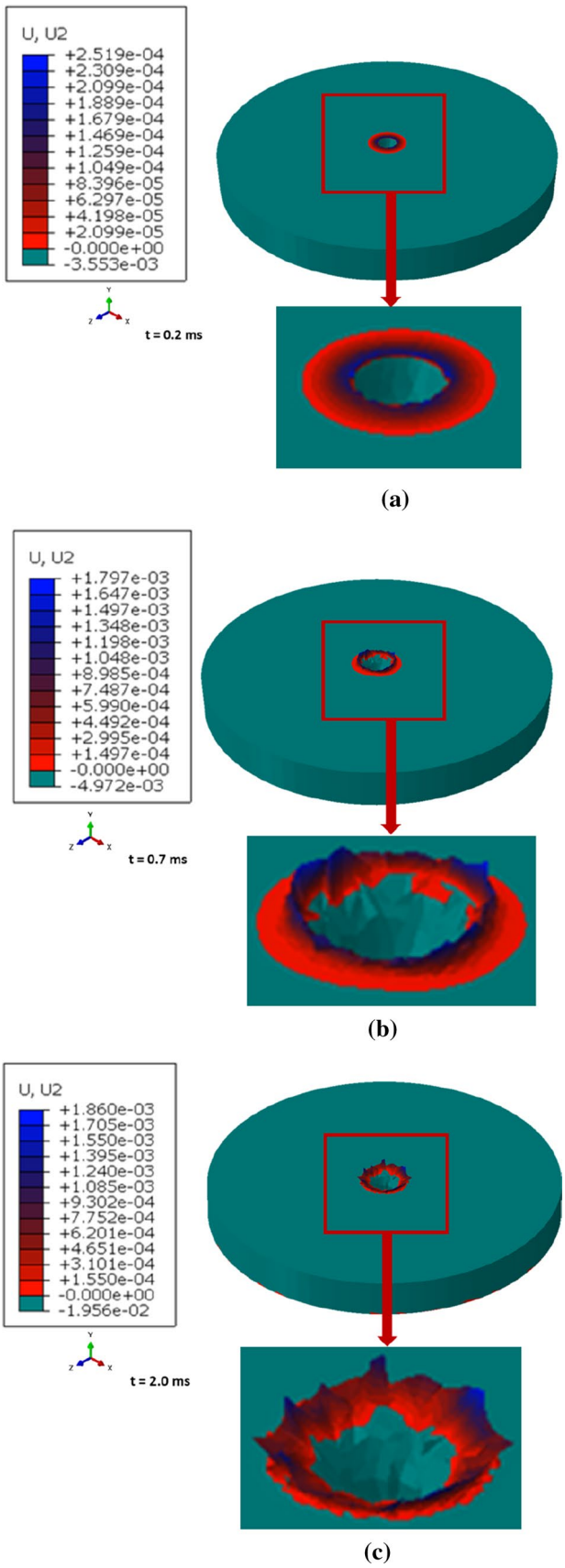

Fig. 13 View of the perforated target-plate showing details of the vertical displacement stages, $U_2 = U_Y$, around the impact zone for the impact velocity equal to $V_i = 15.45$ m/s at: **a** $t = 0.2$ ms; **b** $t = 0.7$ ms and **c** $t = 2.0$ ms

Finally, perforation was attained, Fig. 14c, that was represented by a crater appearance and its subsequent increase due to the impactor movement towards the rear side of the target-plate. The results were obtained for the impact velocity of 15.45 m/s. At time, $t = 2.0$ ms Fig. 14c, the equivalent plastic strain $\bar{\epsilon}^{pl}$ drops from a maximum of 0.92 near the crater edge to a very low value (about 0.05) at a distance of 3.0 mm from the crater edge on the top surface and 12.22 mm from the impactor trajectory on the bottom surface of the target-plate.

4.3 Impactor velocity during perforation

Figure 15 shows the impactor velocity variations determined either in the experiments or numerical simulations. For the time less than 0.6 ms, the numerically calculated values of velocity were close to those in the tests observed, however, one can indicate that, the values of velocity for time greater than 0.6 ms are slightly different than those in experiments achieved.

Figure 16 shows the velocity field distributions in a thickness cross-section of the target-plate under the impactor impact at selected two time intervals, that were determined from the numerical simulations for the impact velocity of $V_i = 15.45$ m/s. Due to the impactor penetration and subsequent perforation a crater appeared on the rear side of the impacted target-plate. Its diameter gradually increased with the impactor penetration.

In Fig. 17 the process of crater diameter increase is presented as a function of time. For low velocity impact it is well approximated by the linear function. Further numerical analysis focused on the equivalent plastic strain and Mises stress distributions on the cross-section through the target-plate impacted by the impactor. It has to be mentioned, that the equivalent plastic strain near the centre of crater reached its critical value at the onset of fracture, $\bar{\epsilon}_f$. Hence, the material points failed, and the fractured elements were removed from the mesh.

4.4 Stress analysis of the AM60 target-plate

A perforation process of the ductile plate of thickness h by a rigid, sharp-nose impactor of mass m_p and nominal diameter $D_p = 2 \cdot r_p$ can be estimated by an energy-balance, e.g. [48]. They showed that the elastoplastic work applied for expanding the perforation cavity can be approximated by $W = \pi \cdot {r_p}^2 \cdot h \cdot \sigma_c$ where σ_c refers to the specific cavitation energy of the target material, also known as an effective

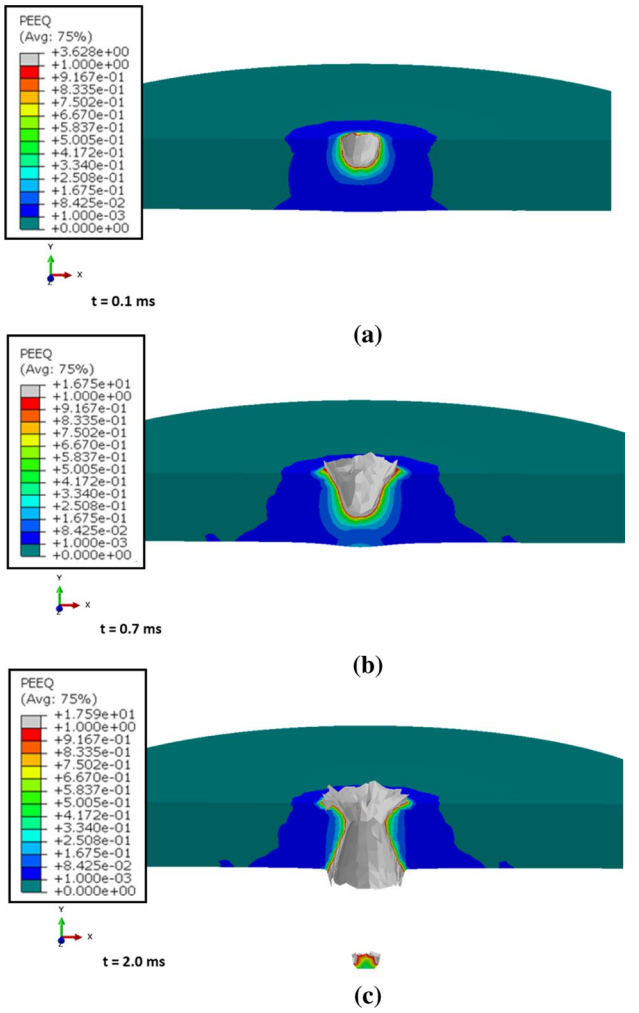

Fig. 14 The equivalent plastic strain field distribution in a thickness cross-section of the target-plate for: **a** $t = 0.1$ ms; **b** $t = 0.7$ ms, **c** $t = 2.0$ ms

resisting stress. The specific cavitation energy depends on the hole slenderness ratio h/D_p and an influence of h/D_p ratio on the ballistic limit demonstrated by [49]. Taking these facts into account, it was estimated by numerical simulations carried out by [48, 50]. The model of Rosenberg and Dekel relates an effective resisting stress $\sigma_c = V_{bl}^2 \cdot \rho_p \cdot L_{\text{eff}}/(2 \cdot h)$ with the ballistic limit velocity V_{bl} of a given impactor/plate pair and the plate's thickness h and the effective length of a mass equivalent right circular cylinder, $L_{\text{eff}} = m_p/(\pi \cdot {r_p}^2 \cdot \rho_p)$ [48]. For the steel impactor used in this study we have $\rho_p \cdot L_{\text{eff}} = 51{,}018$ kg/m^2.

Figure 18 presents variation of the radial stress σ_{11} versus time, calculated numerically for AM60 alloy in case of the impact velocity of $V_i = 15.45$ m/s. The results refer to the finite mesh element located in a distance $l = r_p$ from the central point of impact, where r_p denotes the radius of impactor. The value of σ_{11} is compared with an effective

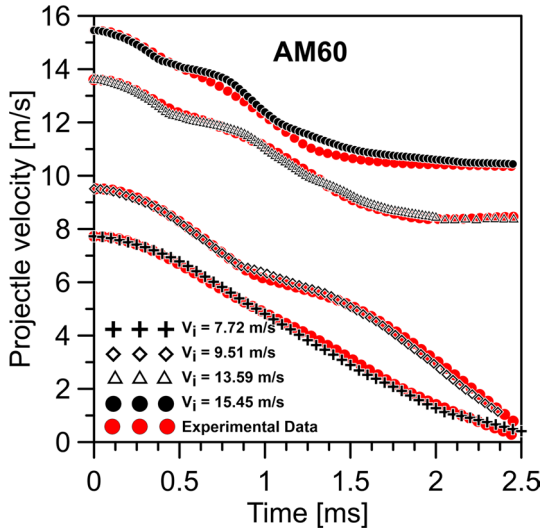

Fig. 15 Numerical model validation: Impact forces versus time determined from numerical calculations (black symbols) and experiments (red symbols)

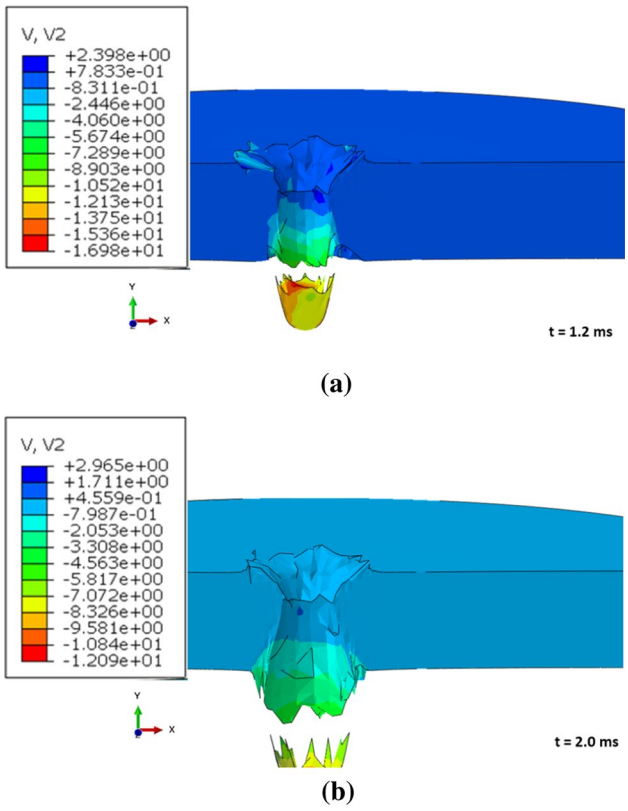

Fig. 16 The velocity field distribution in a thickness cross-section of the target-plate for: **a** $t = 1.2$ ms; and **b** $t = 2.0$ ms. Units are in meter per second

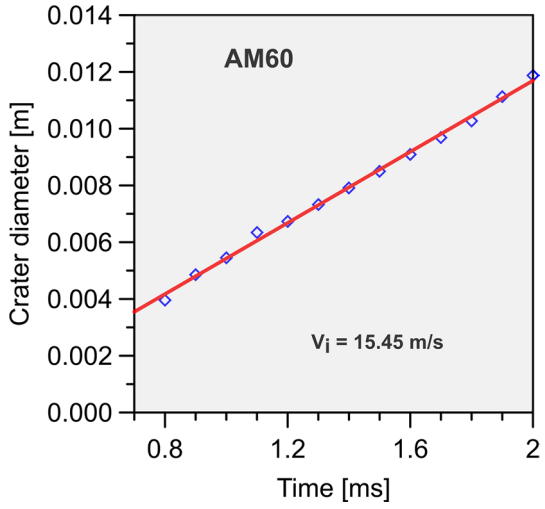

Fig. 17 Crater diameter variation during perforation at the rear side of the target-plate due to the impactor impact for the velocity equal to $V_i = 15.45$ m/s

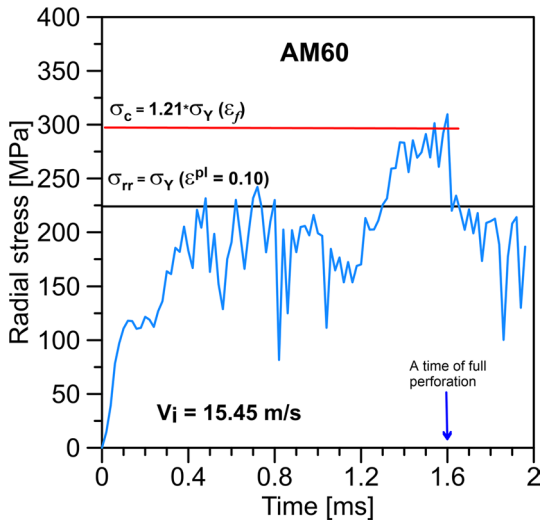

Fig. 18 Radial stress σ_{rr} versus time on the top of the impacted plate in the element located at the distance $l = r_p$ from the main axis of the impactor. The results for the impact velocity of $V_i = 15.45$ m/s

resisting stress $\sigma_c = C \cdot \sigma_Y$ of the Rosenberg and Dekel model, [48]. σ_Y is determined from the quasi-static compression law fit (Fig. 9) at a true strain of 0.1 for which the material was fractured. For the AM60 plate with $h/D_p = 0.833$ the prediction of $\sigma_c = 1.21\sigma_Y(\epsilon_f) = 1.21 \cdot 225$ MPa obtained by the Rosenberg and Dekel model for $0.3 < h/D_p \leq 1$ well corresponds to the numerical calculation.

The Mises stress, σ^{HMH}, field distributions in a thickness cross-section of the plate at $t = 1.2$ ms, and $t = 2.0$ ms are presented in Fig. 19a, b, respectively, for the impact

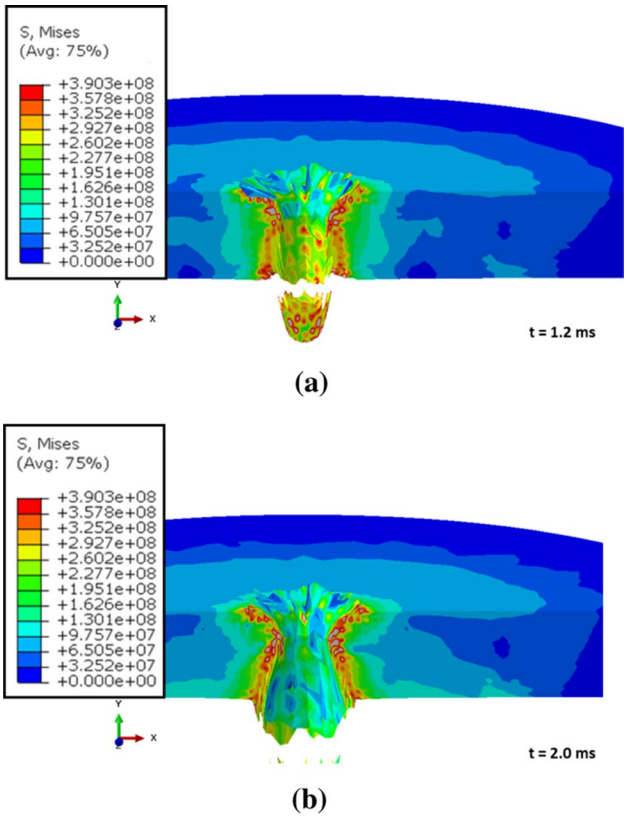

Fig. 19 The Mises stress field distribution in a thickness cross-section of the plate for: **a** $t = 1.2$ ms; and **b** $t = 2.0$ ms

perforation velocity of $V_i = 15.45$ m/s. As it was expected, the maximal values are localised on the wall of hole. The stresses decrease rapidly with distance increase from the central point of impact, and finally attain almost zero level for the distance equal to circa $3 \cdot r_p$, where r_p means a radius of the impactor.

4.5 Energy balance

Among many important issues associated to the impactor impact on the target-plate one can indicate the energy balance problem. A work done by the impactor, W_b, during impact can be defined by the following relationship:

$$W_b = \Delta KE + \Delta FD + \Delta VD + \Delta IE$$

where ΔKE represents the change of the impactor kinetic energy during perforation, Δ FD is the energy dissipated through frictional effects, Δ VD is the energy dissipated through viscous effects associated with volumetric straining and Δ IE describes internal energy change. Δ VD is used to improve the modelling of dynamic events. In our calculation linear bulk viscosity was used.

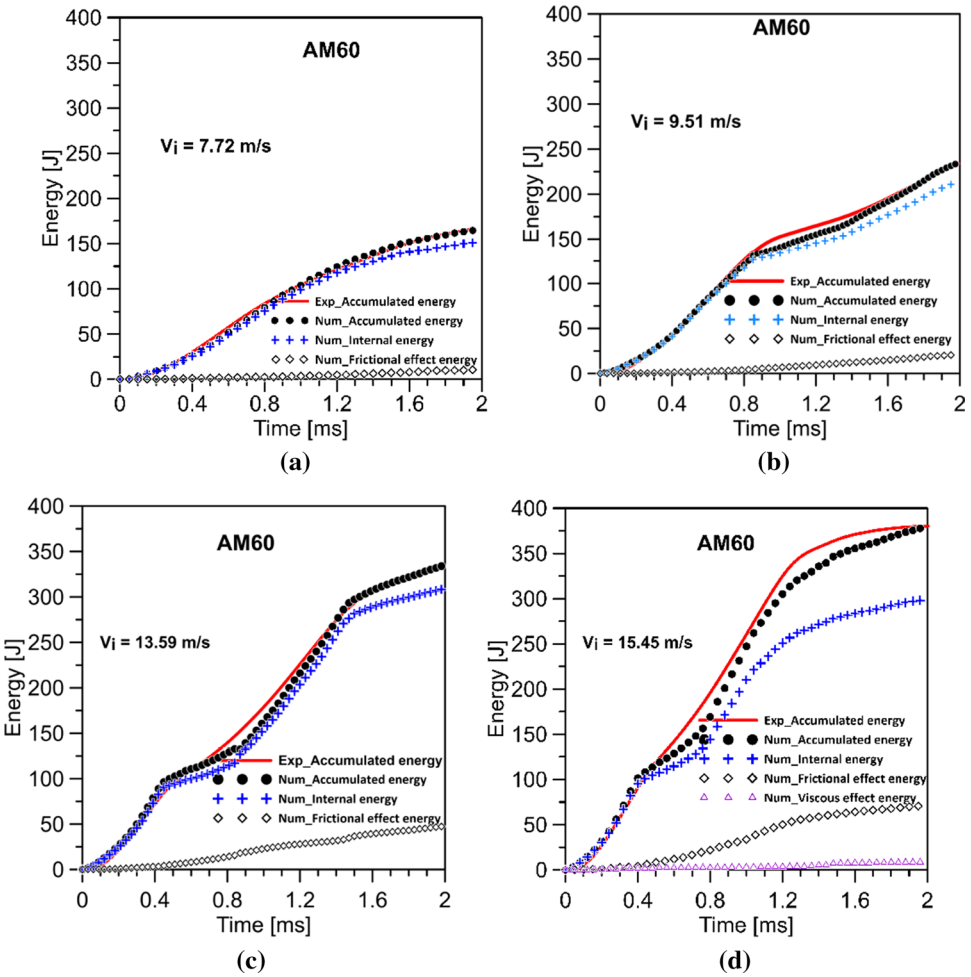

Fig. 20 Numerical model validation: accumulated energy, internal energy, frictional effects energy, versus time-simulations and experiments for the impact velocity of : **a** $V_i = 7.72$ m/s; **b** $V_i = 9.51$ m/s; **c** $V_i = 13.59$ m/s; and **d** $V_i = 15.45$ m/s

The internal energy Δ IE is the sum of energy dissipated during rate-dependent plastic deformation (PD) and the elastic strain energy (SE). When damage occurs in the material, the SE is not entirely recoverable. At any given time, the stress, σ_D, contributing to the SE recovery, that is related to the so-called undamaged stress, σ, can be defined as $\sigma_D = \sigma\,(1 - D)$, where D denotes continuum damage parameter.

Analysis of the energy balance were carried out for selected values of the impact velocity V_i equal to 7.72 m/s, 9.51 m/s, 13.59 m/s and 15.45 m/s. The representative results were presented in Fig. 20a–d. The diagrams show comparison of the numerical predictions to experimental results of the accumulated energy during penetration process enforced by four different values of the impact velocity. It has to be stated that a good agreement between experimental data and numerical simulations was obtained for the low values of impact velocity i.e. $V_i = 7.72$ m/s and $V_i = 9.51$ m/s. For higher ones, a certain scatter can be observed, especially for higher values of the impact velocity and advanced stages of the impactor penetration. Presumably, this situation can be attributed to some thermal effects that were neglected in the model adopted. It has to be emphasised however, that differences identified are relatively small and the model captures a character of the energy variation. Figure 20 also illustrates variations of the numerically calculated internal energy and frictional effect energy as well. Additionally, the viscous effect energy is presented in Fig. 20d. This is because only during the highest impact velocity it could be identified in this research.

5 Summary and concluding remarks

Dynamic behaviour of the commercial polycrystalline AM60 magnesium alloy was studied under low values of impact velocity within the range of 7–16 m/s. Tests were conducted using the conical-nose impactor that penetrated and finally perforated the target-plate. For the impact velocity smaller and equal 9.51 m/s, no residual velocity was observed and the penetration depth was smaller or equal to the plate thickness, and the entire impactor did not pass through the target. For higher values of impact velocity (greater than $V_{bl} = 9.87$ m/s), a residual velocity of the impactor was appeared. The paper was also focused on the flow stress analysis under

quasi-static and dynamic loadings. The deformation generated under low velocity dynamic loading was relatively homogeneous. In order to evaluate deformation of the target-plate, the three-dimensional (3D) non-linear initial-boundary value problem of the low-impact of full metal impactor impacted on the AM60 target-plate was numerically applied within the commercial finite element software ABAQUS/Explicit. The AM60 target plates were modelled as an isotropic elastic-viscoplastic non-linearly strain-hardened material, while the impactor was treated as a rigid material. It was found, that for the impactor incident velocity of 9.51 m/s and kinetic energy of 210 J, the 10 mm thick target-plate was sufficient to stop the impactor penetration of the target-plate. It was observed that the conical-nose impactor left the target-plate with a hole of approximately 11.87 mm diameter. It is important to note that these dimensions remained nearly constant regardless of the variation in the impact velocity for the target plate thickness considered in this study. This also indicates that the fracture induced by the impactor was mostly shear dominated. It can be observed, that peripheral elements around the perforation hole became shortened and more uniform with the increase of the impact velocity. Since the hole size due to perforation was almost constant, 10 mm thickness plate led to increase the plug diameter only slightly. These experimental findings were also replicated in the FE simulation results. The predicted numerically fracture patterns of the AM60 target-plate were compared with those observed in the experiments. Target-plates fracture mechanisms identified in the simulations with ductile damage criterion with and without Lode dependence better matched to the measured force variation than those predicted using the JC-f fracture criterion. In the simulations with fracture criterion the target-plates impacted by the impactor with conical-nose failed through the ductile hole enlargement and its rear side circumferential fracture creating petals. A detailed analysis of the AM60 punching revealed, that in case of the low velocity impact with conical-nose impactor, the ductile hole enlargement occurred during the initial stage of the impact, and subsequently, through-thickness fracture developed causing its shear plugging failure. The JC-f fracture criterion overestimated the measured force response, thus, providing to a rather poor prediction of the target plate impact performance in the numerical simulations. It has to be mentioned, that the simulation with the use of Lode-independent JC-f fracture criterion can be replaced by the Lode-dependent modified Mohr–Coulomb (MMC) fracture criterion extended through JC strain-rate and temperature terms, similarly as in [51]. JC model parameters for AM60 magnesium alloy are identified based on dynamic uniaxial tests to fit the experimental impact velocity within the range of 7–16 m/s at room temperature. The parameters values presented in Table 5 (Model parameters for AM60) are obtained under assumption of no influence of the temperature softening on the perforation mechanisms for the whole range of impact velocities considered. The parameter reflecting thermal softening effects, m, and one of the damage law parameter (D_5) are equal zero according to a simplified model of perforation. Thus, the results in term of impact force, impact energy, impactor displacement and velocity are obtained. In the case of high velocity impact processes, infrared measurements of the temperature increase in the material can be especially useful to study the influence of adiabatic heating on strength, ductility and impact energy of the AM60 magnesium alloys.

Acknowledgements The work was partly supported by the project no. PPI/APM/2018/1/00045/U/001 financed by the Polish National Academic Exchange Agency.

Author Contributions ZN: conceptualization, methodology, validation, formal analysis, investigation, writing—original draft. ZLK: supervision, conceptualization, methodology, validation, formal analysis, investigation, writing—review and editing. TS: Data curation, Validation, formal analysis, investigation, writing—review.

Declarations

Conflict of interest The authors declared that they have no conflicts of interest to this work. We declare that we do not have any commercial or associative interest that represents a conflict of interest in connection with the work submitted. The authors declare that they have no known competing financial interests or personal relationships that could have appeared to influence the work reported in this paper.

Ethical approval The authors declare that the research was conducted according to the ethical standards.

References

1. Arias A, Rodríguez-Martínez JA, Rusinek A. Numerical simulations of impact behaviour of thin steel plates subjected to cylindrical, conical and hemispherical non-deformable projectiles. Eng Fract Mech. 2008;75:1635–56.
2. Iqbal MA, Gupta G, Diwakar A, et al. Effect of projectile nose shape on the ballistic resistance of ductile targets. Eur J Mech A/Solids. 2010;29:683–94.
3. Dey S, Børvik T, Hopperstad OS, et al. The effect of target strength on the perforation of steel plates using three different projectile nose shapes. Int J Impact Eng. 2004;30(8–9):1005–38.

4. Kane A, Børvik T, Hopperstad OS, et al. Finite element analysis of plugging failure in steel plates struck by blunt projectiles. J Appl Mech. 2009;76:051302–1–11.
5. Mohr D, Marcadet SJ. Micromechanically-motivated phenomenological Hosford-Coulomb model for predicting ductile fracture initiation at low stress triaxialities. Int J Solids Struct. 2015;68:40–55.
6. Kula A, Tokarski T, Niewczas M. Comparative studies on the structure and properties of rapidly solidified and conventionally cast AM60 magnesium alloys. Mater Sci Eng A. 2019;759:346–56.
7. Prasad KE, Li B, Dixit N, et al. The dynamic flow and failure behavior of magnesium and magnesium alloys. JOM. 2014;66(2):291–304.
8. Kondori B, Mahmudi R. Effect of Ca additions on the microstructure, thermal stability and mechanical properties of a cast AM60 magnesium alloy. Mater Sci Eng A. 2010;527:2014–21.
9. Magliaro J, Altenhof W. Energy absorption mechanisms and capabilities for magnesium extrusions under impact. Int J Mech Sci. 2020;179: 105667.
10. Malik A, Wang Y, Huanwu C, et al. Dynamic mechanical behavior of magnesium alloys: a review. Int J Mater Res. 2019;110(12):1105–15.
11. Wang M, Lu L, Li C, et al. Deformation and spallation of a magnesium alloy under high strain rate loading. Mater Sci Eng A. 2016;661:126–35.
12. Li Q. Dynamic compressive mechanical behavior of magnesium-based materials: magnesium single crystal, polycrystalline magnesium, and magnesium alloy Handbook of mechanics of materials. Singapore: Springer; 2019. p. 845–72.
13. Wierzbicki T. Petalling of plates under explosive and impact loading. Int J Impact Eng. 1999;22:935–54.
14. Rusinek A, Rodríguez-Martínez JA, Zaera R, et al. Experimental and numerical study on the perforation process of mild steel sheets subjected to perpendicular impact by hemispherical projectiles. Int J Impact Eng. 2009;36:565–87.
15. Simulia ABAQUS/Explicit User's Manual Version 6.16 Edition. Dassault Systems, Providence. 2016.
16. Szymczak T, Makowska K, Kowalewski ZL, et al. An influence of impact energy on magnesium alloy behaviour. Int J Mech Mater Des. 2020;16:139–53.
17. Recht RF, Ipson TW. Ballistic perforation dynamics. J Appl Mech. 1963;30(3):384–90.
18. Lambert JP, Jonas GH. Towards standardization in terminal ballistics testing: velocity representation. Aberdeen Proving Grounds, MD: BRL-R-1852 U.S. Army Ballistics Research Laboratory, USA; 1976.
19. Rodríguez-Martínez JA, Pesci R, Rusinek A, et al. Thermo-mechanical behaviour of TRIP 1000 steel sheets subjected to low velocity perforation by conical projectiles at different temperatures. Int J Solids Struct. 2010;47:1268–84.
20. Rodríguez-Martínez JA, Rusinek A, Pesci R. Experimental survey on the behaviour of AISI 304 steel sheets subjected to perforation. Thin-Wall Struct. 2010;48:966–78.
21. Rosenberg Z, Vayig Y. On the friction effect in the perforation of metallic plates by rigid projectiles. Int J lmpact Eng. 2021;149: 103794.
22. Sannes S, Gjestland H, Westengen H, et al. Die casting of magnesium alloys—the importance of controlling die filling and solidification. SAE Trans. 2003;112:1–9.
23. Song WQ, Beggs P, Easton M. Compressive strain-rate sensitivity of magnesium-aluminum die casting alloys. Mater Des. 2009;30(3):642–8.
24. Dudamell NV, Galvez F, Perez-Prado MT. Dynamic deformation of high pressure die-cast magnesium alloys. Rev Metal. 2012;48(5):351–7.
25. Gu G, Lin S, Meng Y, et al. Influence of strain rate and stress state on the mechanical behavior of die-casting AM60 magnesium alloy. Proc ASME Int Mech Eng Congress Expos. 2011;8(11):425–33.
26. Gu G, Lin S, Xia Y, et al. Experimental study on influence of section thickness on mechanical behavior of die-cast AM60 magnesium alloy. Mater Des. 2012;38:124–32.
27. Aune TK, Albright D, Westengen H, et al. Behavior of die cast magnesium alloys subject to rapid deformation. SAE Trans. 2000;109:555–9.
28. Dørum C, Hopperstad OS, Langseth M, et al. Energy absorption capacity for hpdc components. SAE Trans. 2004;113:1–6.
29. Kraehling D. Effect of stress triaxiality on constitutive response and failure of super vacuum die cast AM60B magnesium alloy. Master of Applied Science thesis, Mechanical Engineering Waterloo University, Ontario, Canada; 2014.
30. Weiler JP, Wood JT, Klassen RJ, et al. Relationship between internal porosity and fracture strength of die-cast magnesium AM60B alloy. Mater Sci Eng A. 2005;395:315–22.
31. Hebben R. The material and its properties. magnesium diecasting. STIHL folder pp 1–4; 2010. https://magnesium.stihl.com/p/media/download/d4/material_and_properties.pdf
32. Yan C, Bai RX, Gu YT, et al. Investigation on mechanical behaviour of AM60 magnesium alloys. J Achiev Mater Manuf Eng. 2008;31(2):398–401.
33. Buch A. Asm specialty handbook—magnesium and magnesium alloys. Metals Park: ASM International; 1999. p. 22–49.
34. Lubliner J. Plasticity theory. New York: Springer; 1990.
35. Johnson GR, Cook WH. Fracture characteristics of three metals subjected to various strains, strain rates, temperatures and pressures. Eng Fract Mech. 1985;21(1):31–48.
36. Cao J, Lin J. A study on formulation of objective functions for determining material models. Int J Mech Sci. 2008;50(2):193–204.
37. Yao D, Duan Y, Li M, et al. Hybrid identification method of coupled viscoplastic-damage constitutive parameters based on BP neural network and genetic algorithm. Eng Fract Mech. 2021;257: 108027.
38. Jia Y, Bai Y. Ductile fracture prediction for metal sheets using all-strain-based anisotropic eMMC model. Int J Mech Sci. 2016;115–116:516–31.
39. Lou Y, Chen L, Clausmeyer T, et al. Modeling of ductile fracture from shear to balanced biaxial tension for sheet metals. Int J Solids Struct. 2017;112:169–84.
40. Teng X, Wierzbicki T. Evaluation of six fracture models in high velocity perforation. Eng Fract Mech. 2006;73(12):1653–78.
41. Torki M, Keralavarma S, Benzerga A. An analysis of Lode effects in ductile failure. J Mech Phys Solids. 2021;153: 104468.
42. Perzyna P. Thermodynamic theory of viscoplasticity. Adv Appl Mech. 1971;11:313–54.
43. Simó JC, Hughes TJR. Computational inelasticity. NewYork: Springer; 1998.
44. Voyiadjis GZ, Abed FH. Transient localizations in metals using microstructure based yield surfaces. Model Simul Mater Sci Eng. 2006;15(1):S83.
45. Backman ME, Goldsmith W. The mechanics of penetration of projectiles into targets. Int J Eng Sci. 1978;16(1):1–99.
46. Feldgun VR, Yankelevsky DZ, Karinski YS. Cavitation phenomenon in penetration of rigid projectiles into elastic-plastic targets. Int J lmpact Eng. 2021;151: 103837.
47. Masri R. Low-velocity penetration of a rigid, hemispherical nose projectile in incompressible, elastoplastic, strain-hardening mises media. Int J Solids Struct. 2019;167:14–23.
48. Rosenberg Z, Dekel E. Revisiting the perforation of ductile plates by sharp-nosed rigid projectiles. Int J Solids Struct. 2010;47:3022–33.

49. Ryan S, Nguyen LH, Gallary D, et al. A scaling law for predicting the ballistic performance of aluminum alloy targets perforated in ductile hole formation. Int J lmpact Eng. 2018;116:34–50.
50. Rosenberg Z, Dekel E. On the deep penetration and plate perforation by rigid projectiles. Int J Solids Struct. 2009;46:4169–80.
51. Wang Y, Chen X, Xiao X, et al. Effect of Lode angle incorporation into a fracture criterion in predicting the ballistic resistance of 2024–T351 aluminum alloy plates struck by cylindrical projectiles with different nose shapes. Int J lmpact Eng. 2020;139: 103498.